RAA 2016 Vol. **16** No. **11**, 167 (10pp) doi: 10.1088/1674–4527/16/11/167
© 2016 National Astronomical Observatories, CAS and IOP Publishing Ltd.
http://www.raa-journal.org *http://iopscience.iop.org/raa*

***R**esearch in*
***A**stronomy and*
***A**strophysics*

Damped large amplitude oscillations in a solar prominence and a bundle of coronal loops

Quan-Hao Zhang[1], Yu-Ming Wang[1,2], Rui Liu[1,3], Cheng-Long Shen[1,2], Min Zhang[1,4,5], Ting-Yu Gou[1,4], Jia-Jia Liu[1], Kai Liu[1], Zhen-Jun Zhou[1,4] and Shui Wang[1]

[1] CAS Key Laboratory of Geospace Environment, Department of Geophysics and Planetary Sciences, University of Science and Technology of China, Hefei 230026, China; *zhangqh@mail.ustc.edu.cn, ymwang@ustc.edu.cn*
[2] Synergetic Innovation Center of Quantum Information & Quantum Physics, University of Science and Technology of China, Hefei 230026, China
[3] Collaborative Innovation Center of Astronautical Science and Technology, Hefei 230026, China
[4] Mengcheng National Geophysical Observatory, School of Earth and Space Sciences, University of Science and Technology of China, Hefei 230026, China
[5] Department of Mathematics and Physics, Anhui Jianzhu University, Hefei 230601, China

Received 2016 March 13; accepted 2016 June 27

Abstract We investigate the evolutions of two prominences (P1, P2) and two bundles of coronal loops (L1, L2), observed with *SDO*/AIA near the east solar limb on 2012 September 22. It is found that there were large-amplitude oscillations in P1 and L1 but no detectable motions in P2 and L2. These transverse oscillations were triggered by a large-scale coronal wave, originating from a large flare in a remote active region behind the solar limb. By carefully comparing the locations and heights of these oscillating and non-oscillating structures, we conclude that the propagating height of the wave is between 50 Mm and 130 Mm. The wave energy deposited in the oscillating prominence and coronal loops is at least of the order of 10^{28} erg. Furthermore, local magnetic field strength and Alfvén speeds are derived from the oscillating periods and damping time scales, which are extracted from the time series of the oscillations. It is demonstrated that oscillations can be used in not only coronal seismology, but also to reveal the properties of the wave.

Key words: Sun: filaments, prominences — Sun: flares — Sun: oscillations — waves

1 INTRODUCTION

Prominence (filament) oscillations have been observed for a long time (e.g. Kleczek & Kuperus 1969). They are classified into two groups based on their velocity amplitudes: large-amplitude oscillations with velocity amplitude $\geq$20 km s^{-1} (Tripathi et al. 2009) and small-amplitude oscillations with velocity amplitude 2–3 km s^{-1} (Oliver & Ballester 2002; Arregui et al. 2012). In earlier observations, large-amplitude oscillations were caused by Moreton waves (Gilbert et al. 2008; Liu et al. 2013), coronal waves (Okamoto et al. 2004; Hershaw et al. 2011; Liu et al. 2012) and nearby flares or jets (Vršnak et al. 2007; Li & Zhang 2012). The recent observation by Zhang et al. (2014) revealed that rising chromospheric fibrils merged with a prominence and triggered the prominence to oscillate in large amplitude. This process, which is named "flux feeding," is also a possible trigger of large-amplitude oscillations. So far, there are few observations of large-amplitude oscillations in prominences triggered by waves. With the method of prominence seismology, local physical parameters, such as magnetic field strength, can be extracted from the properties of the oscillations (Isobe & Tripathi 2006; Vršnak et al. 2007; Oliver 2009). By analyzing the oscillation of a prominence during its slow rise phase, Isobe et al. (2007) concluded that prominence seismology based on large-amplitude oscillation can also be a diagnostic tool for stability and the eruption mechanism of the prominence.

Oscillations are also found in coronal loops. Damped oscillations in coronal loops were first discovered by the EUV telescope on board the *Transition Region and Coronal Explorer (TRACE)* spacecraft (Aschwanden et al. 1999; Nakariakov et al. 1999), and then further discussed by Schrijver et al. (2002) and Aschwanden et al. (2002). Nakariakov et al. (1999) concluded that all parts of the loop oscillated transversely and in phase, indicating a kink global standing mode of the loop. There are several damping mechanisms for kink oscillations in coronal loops, such as footpoint or side energy leakage (Schrijver & Brown 2000), phase mixing (Heyvaerts & Priest 1983; Roberts

2000) and resonant absorption (Ruderman & Roberts 2002; Ruderman 2005). It is still an open question as to which mechanisms are working in the damping process. Physical parameters of the oscillations, e.g. periods and damping times, can be used to obtain indirect information on the conditions of the plasma and magnetic field in coronal loops (Nakariakov & Ofman 2001; Goossens et al. 2002; Arregui et al. 2007).

Large-scale coronal waves were first observed by the Extreme ultraviolet Imaging Telescope (EIT; Delaboudinière et al. 1995) on board the *Solar and Heliospheric Observatory* (*SOHO*; Thompson et al. 1999), and hence are also called "EIT waves." In some papers, coronal waves are also introduced as "EUV waves," corresponding to the same phenomena. Coronal waves are commonly interpreted as fast magnetosonic waves (Wang 2000; Ofman & Thompson 2002), which are always associated with a flare, usually propagating from the flare site isotropically at a typical speed of $200-500$ km s^{-1} (Nakariakov & Verwichte 2005). The properties of the wave vary during propagation because of the interaction with coronal magnetic structures (Ofman & Thompson 2002; Gopalswamy et al. 2009; Veronig et al. 2010). Studies of coronal waves have shed light on fundamental physical problems in solar physics, such as acceleration of the fast solar wind (Cranmer et al. 2007) and the mechanism of coronal heating (Heyvaerts & Priest 1983). There are close relationships between coronal waves and oscillations of coronal structures. On one hand, a coronal wave is a possible trigger of the oscillations (Hershaw et al. 2011; Kumar et al. 2013), and on the other hand the oscillating parameters reveal the physical properties of both the wave and the oscillating structures (Gilbert et al. 2008).

In this paper, we study the oscillations of a prominence and a bundle of coronal loops associated with the coronal wave generated by a large flare. The different parameters of the oscillating and non-oscillating structures reveal the propagation properties of the coronal wave. In the following sections, we establish the locations of the relevant prominences and coronal loops through multi-spacecraft observations (Sect. 3.1) to investigate the interaction between the wave and magnetic structures (Sect. 3.2), calculate the oscillating properties of the oscillating structures (Sect. 3.3), and estimate the local magnetic field strength and Alfvén speed from the oscillating properties (Sect. 3.4). By comparing the locations of the structures, we roughly estimate the propagating height of the wave (Sect. 3.5). Finally, a discussion and conclusion are given in Section 4.

2 INSTRUMENT AND DATA

The prominences and the coronal loops were observed off the east limb in EUV by the Atmospheric Imaging Assembly (AIA; Lemen et al. 2012) on board the *Solar Dynamics Observatory* (*SDO*; Pesnell et al. 2012). Images taken by the Extreme Ultraviolet Imager (EUVI; Wuelser et al. 2004), which is part of the Sun Earth Connection Coronal and Heliospheric Investigation (SECCHI; Howard et al. 2008) imaging package on board the *Solar TErrestrial RElations Observatory* (*STEREO*; Kaiser et al. 2008), are utilized to investigate the propagation of the coronal wave. The prominences appeared as dark filaments in the field of view (FOV) of *STEREO*'s 'Behind' spacecraft (*STB*). Two prominences and two bundles of magnetic coronal loops are analyzed in this paper.

Table 1 Geometrical Parameters

	D (Mm)*	H (Mm)	L (Mm)**	Oscillate or not
P1	490^{+80}_{-120}	130	220	Y
P2	550^{+80}_{-150}	50	80	N
L1	360^{+70}_{-100}	210	220	Y
L2	930^{+140}_{-190}	200	320	N

* The superscripts and subscripts correspond to the spatial range of the structures.

** L is the estimated length of the parts that can be reconstructed in 3D.

3 OBSERVATIONS

3.1 3D Reconstruction of the Structures

Figure 1 illustrates the locations of the relevant prominences and loops from the perspectives of both the *SDO* and *STEREO* satellites, the positions of which are shown by the inset in Figure 1(b). Figure 1(a) is the running ratio image of EUVI 304 Å observations, and Figure 1(b) is the original AIA 304 Å image. There are two prominences located at almost the same region in Figure 1(a), apparently intersecting with each other (also see the animation accompanying Fig. 1), but in fact they are suspended at different heights, as shown in Figure 1(b). The higher prominence, spreading along the direction from northeast to southwest in Figure 1(a), is labeled as 'P1,' and the lower prominence, generally in the east-to-west direction but turning northward at its west end, is labeled as 'P2.' P1 and P2 can be clearly recognized in the animation accompanying Figure 1. Figure 1(c) and 1(d) are the linearly scaled 171 Å original images from EUVI and AIA, respectively. There is a bundle of coronal loops appearing as a bright dome, which is labeled as 'L2.' Different scalings are used in different regions in Figure 1(c), so as to clearly reveal different parts of L2. Figure 1(e) is the running difference image of EUVI 195 Å observations, and Figure 1(f) is the running difference of AIA 193 Å images. Another bundle of coronal loops is observed here, called 'L1' hereafter. It appears as a dark arch in Figure 1(e) and 1(f), as pointed out by the red arrow. L1 is nearer to the flare site than L2. Different from L2, only after the onset of the flare and the passage of a coronal wave would L1 be visible in the FOV of *STB* (see the animation accompanying Fig. 1), resulting from the oscillating motions triggered by the wave (see Sect. 3.3).

Observations from different perspectives make it possible to build 3D reconstructions of these structures. Here we use SCC_MEASURE in the Solar Software package to analyze the 3D geometric properties of the structures.

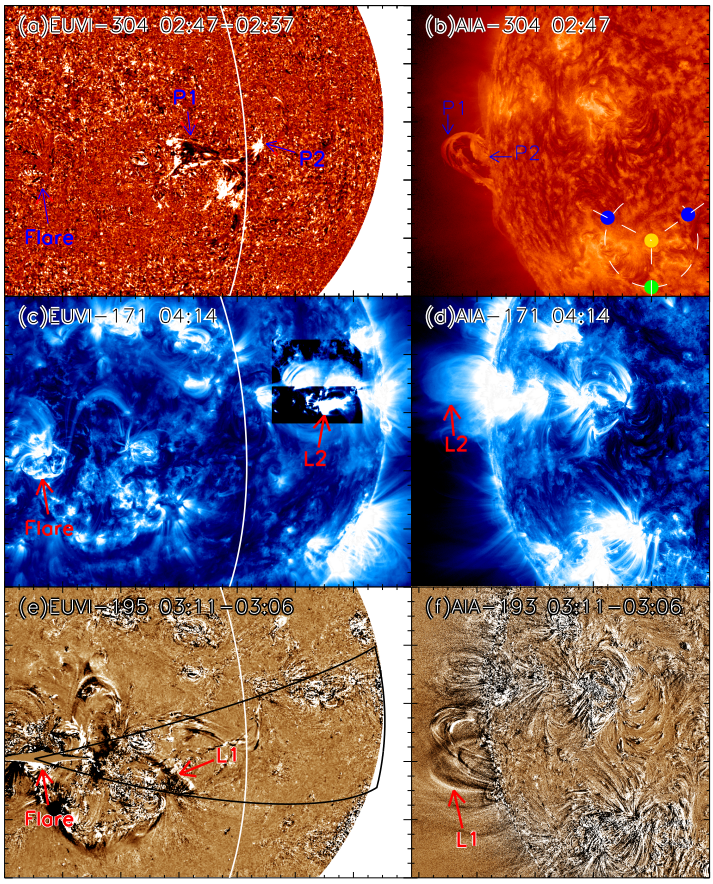

Fig. 1 The locations of the prominences and coronal loops analyzed in this paper. The left panels are images taken by *STB*/EUVI and the right panels are taken by *SDO*/AIA. The white curves in the left panels denote the solar limb as seen by *SDO*. Panel (a) is the running ratio image of EUVI 304 Å observations; panel (b) is the AIA 304 Å original image, and the inset plots the positions of the *STEREO* spacecrafts (*blue dots*) relative to the Sun (*yellow dot*) and the Earth (*green dot*) in the plane of Earth's orbit, with *STEREO*-A ahead of, and *STB* behind, the Earth. Panels (c) and (d) are the scaled 171 Å original images from EUVI and AIA, respectively. In panel (c), in order to clearly show the profile of L2, different scalings are used in different regions. Panel (e) is the running difference image of EUVI 195 Å observations, and panel (f) is that of AIA 193 Å. The prominences and the loops are marked as P1, P2, L1 and L2. The solid black lines in the bottom left panel trace the region covering both P1 and L1, whose center is located at the flare site.

The results are shown in Figure 2, where the reconstructed points of P1, P2 and L1 are marked by blue cross symbols, cyan cross symbols and red pluses, respectively. The geometric parameters of these relevant structures, obtained from the 3D reconstructions, are tabulated in Table 1: D is the mean distance from the flare site, with the superscripts and subscripts indicating the spatial ranges of the structures, H is the maximum 3D height and L is the estimated 3D length of the structures, which is calculated by summing the 3D distances of neighboring reconstructed points by SCC_MEASURE. It should be noted that L only represents the length of the parts of the structures that could be clearly recognized in the FOVs of both *SDO* and *STEREO*. Obviously, the estimated L is the lower limit of the actual length. The white curves in the left panels trace the solar limb as seen by *SDO*. It is obvious that P1, P2 and L2 were located near or to the west of (in front of) the solar limb in *SDO*, indicating that most parts of P1, P2 and L2 could be tracked in the 3D reconstruction. The coronal loops L1, however, were located more distant from the solar limb in *SDO*. As a result, some lower parts of L1 were occulted by the solar disk from the perspective of *SDO*, which explains that its visible part in *SDO* has a minimum 3D height of 88 Mm. For comparison, the minimum tracked 3D heights of P1, P2 and L2 are only 15, 20 and 6 Mm, respectively. Therefore, the calculated length from the 3D reconstruction for L1 is far from accurate; although the calculated lengths for P1, P2 and L2 are also underestimated, the deviations should not be large.

3.2 Overview of the Event

A big flare erupted at about 03:00 UT on 2012 September 22, corresponding to the vertical solid lines in Figure 3(d)-3(h). The flare generated a large-scale coronal wave, triggering the oscillations of prominence P1 and coronal loops L1 (also see the animation accompanying Fig. 3). The wave front can be tracked in the EUVI 195 Å running difference image, as marked by the white cross symbols in Figure 3(e). Figure 3(f) and 3(h) is the space-time stack

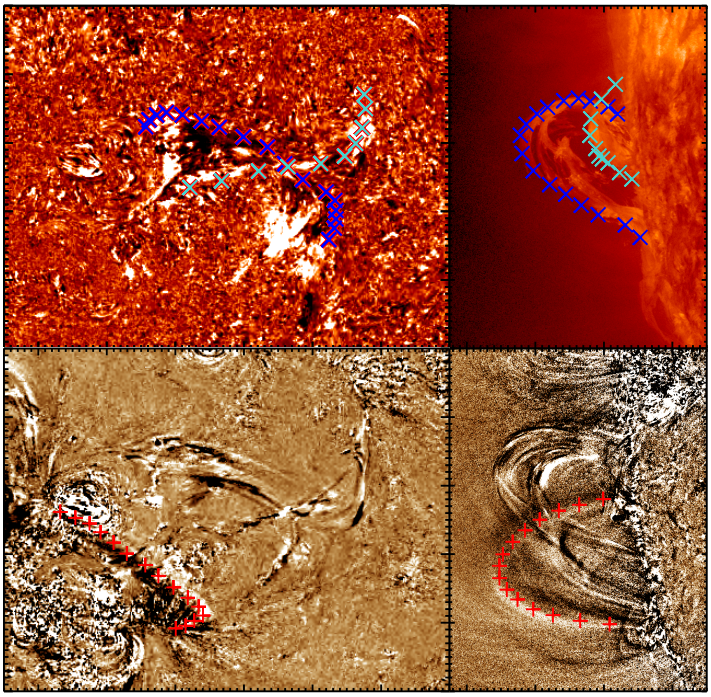

Fig. 2 3D reconstructed results of P1, P2 and L1. The images are the same as those in Fig. 1(a), 1(b), 1(d) and 1(f), but zoom in on the region of P1, L1 and L2. The 3D reconstructed points of P1 are marked by blue cross symbols, P2 by cyan cross symbols and L1 by red pluses.

plots generated from EUVI 195 Å running difference images in the sector regions Sec-P and Sec-L in Figure 3(c), respectively. The centers of these sector regions are both located at the flare site. In comparison with Figure 1, it is revealed that Sec-P is across the region of the prominences, and Sec-L is across the region of L1. The horizontal red and blue lines in Figure 3(f) and 3(h) indicate the locations of the prominence P1 and the loops L1 respectively. The wave front, which is marked by the white cross symbols in Figure 3(c), can also be recognized in Figure 3(f) and 3(h), as marked by the white cross symbols. The propagating velocities of the coronal wave are obtained by a linear fitting: (440±9) km s^{-1} along Sec-P and (560±2) km s^{-1} along Sec-L, indicating that it should be a fast wave. The velocity of the wave was almost constant during its propagation, so that the arrival times of the wave at the locations of P1 and L1 are calculated to be 03:11 UT for P1 and 03:07 UT for L1, denoted by the vertical dotted line in Figure 3(d)-3(f) and the vertical dashed line in Figure 3(g)-3(h), respectively. Both the prominence threads and the coronal loops began to oscillate with the wave passage, indicating that the oscillations were indeed triggered by the coronal wave.

3.3 Oscillating Parameters

Figure 3(d) and 3(e) is the space-time stack plots illustrating the motion in P1, generated from Slit-1 (see Fig. 3(a) or Fig. 3(b)). Figure 3(d) is obtained from AIA 304 Å original images, and Figure 3(e) from AIA 193 Å base difference images. During the pre-flare phase, P1 rose upwards almost as a whole, and then was suspended in the corona with an arch-like shape. The prominence was stabilized presumably by the overlaying arcades (see Fig. 4), and prominence material was observed to fall back to the surface. Apart from the motion of the prominence as a whole, some threads of P1 also began to oscillate transversely to the prominence spine at about 03:11 UT, immediately after the wave passage. The oscillation of the prominence threads, marked by green dots, can be well-fitted with a damped cosine function with an initial height h_0, velocity v_0 and acceleration a_0

$$h(t) = h_0 + v_0 t + \frac{a_0}{2} t^2 + A\cos\left(\frac{2\pi}{T}t + \phi\right)\mathrm{e}^{-t/\tau}, \quad (1)$$

where A, T and τ correspond to the amplitude, period and e-folding damping time, respectively. The height h is measured from Figure 3(d), and the error of h is selected to be the length of 5 pixels in the image, $\Delta h \approx 2.2$ Mm. The fitting yields $v_0 = (21 \pm 1)$ km s^{-1}, $a_0 = (6.2 \pm 0.6)$ m s^{-2}, $A = (5.7 \pm 1.0)$ Mm, $T = (1000 \pm 20)$ s and $\tau = (2500 \pm 900)$ s. The velocity amplitude is calculated to be (35 ± 7) km s^{-1}, which is part of the large-amplitude oscillation. Separate from the damped oscillation, the non-oscillating part of this prominence was still undergoing a slow rise, as marked by the white dots. With a linear fitting, the slow rise velocity is calculated to be $v_0 = (3.6 \pm 0.1)$ km s^{-1}. Different from P1, P2 was non-oscillating, with no obvious motions along the slit, as shown in Figure 3(d) and (e).

Figure 3(g) is the stack plot generated from AIA 193 Å base difference images along Slit-2 in Figure 3(b), which reveals the transverse oscillation of L1. The coronal loops

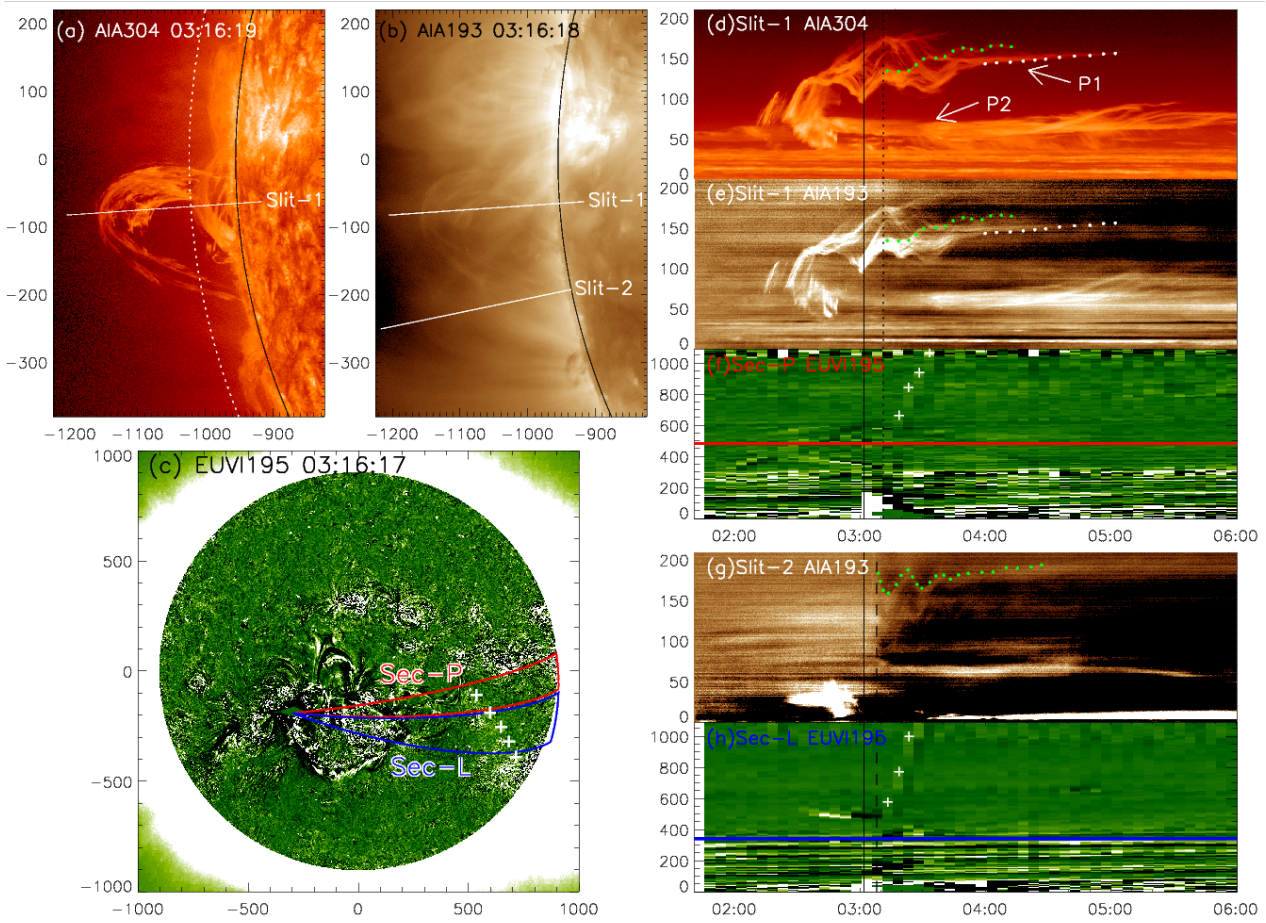

Fig. 3 Analysis of the oscillations and the wave. Panels (a) and (b) show a 304 Å image and a 193 Å image respectively, with two virtual slits, Slit-1 and Slit-2, perpendicular to the solar surface; panel (c) is a 195 Å running difference image, with two regions marked as Sec-P and Sec-L, whose centers are both located at the flare region, and the wave front is marked by white cross symbols; panel (d) is the space-time stack plot obtained from the original 304 Å images along Slit-1 in panel (a), and panel (e) is from 193 Å base difference images along slit 1; panel (g) is the stack plot from 193 Å base difference images along Slit-2 in panel (b); panels (f) and (h) are stack plots from 195 Å running difference images along Sec-P and Sec-L in panel (c), respectively. The wave structures are marked by cross symbols in panels (f) and (h). The green dots in panels (d), (e) and (g) represent the oscillating prominence thread and coronal loops. The red solid line in panel (f) and the blue one in panel (h) correspond to the locations of the prominence P1 and the coronal loops L1, respectively. The white dotted curve in panel (a) indicates the height of 50 Mm.

also began to oscillate immediately after the wave passage at about 03:07 UT. The coronal loops oscillated transversely as a whole, indicating a cylindrical kink mode (also see the animation accompanying Fig. 3). The oscillation of the coronal loop is outlined by the green dots in Figure 3(g). A damped cosine function with a uniformly slow rising velocity v_0 is used here to fit the oscillation of L1

$$h(t) = h_0 + v_0 t + A\cos\left(\frac{2\pi}{T}t + \phi\right)\mathrm{e}^{-t/\tau}. \qquad (2)$$

The fitting yields $v_0 = (4.8 \pm 0.2)$ km s^{-1}, $A = (20 \pm 1)$ Mm, $T = (960 \pm 10)$ s and $\tau = (1300 \pm 100)$ s. The velocity amplitude is about (130 ± 10) km s^{-1}. The oscillating periods of the prominence threads and the coronal loops are approximately the same.

3.4 Estimating the Magnetic Field

In order to calculate the magnetic field from the oscillating parameters, the densities within the oscillating prominence and coronal loops should first be estimated, which is achieved by differential emission measures (DEMs; Hannah & Kontar 2012). Figure 5 demonstrates the distribution of the emission measure (hereafter, EM), obtained from the integral of the DEM results. The relationship between EM and electron density is written as

$$\mathrm{EM} = n^2 d, \qquad (3)$$

where n is the electron density and d is the column depth along the line of sight (LOS) (Aschwanden & Acton 2001). The distribution of logarithmic EM is shown in Figure 5(a); the corresponding AIA 193 Å running difference image is shown in Figure 5(b). We select a square region around L1

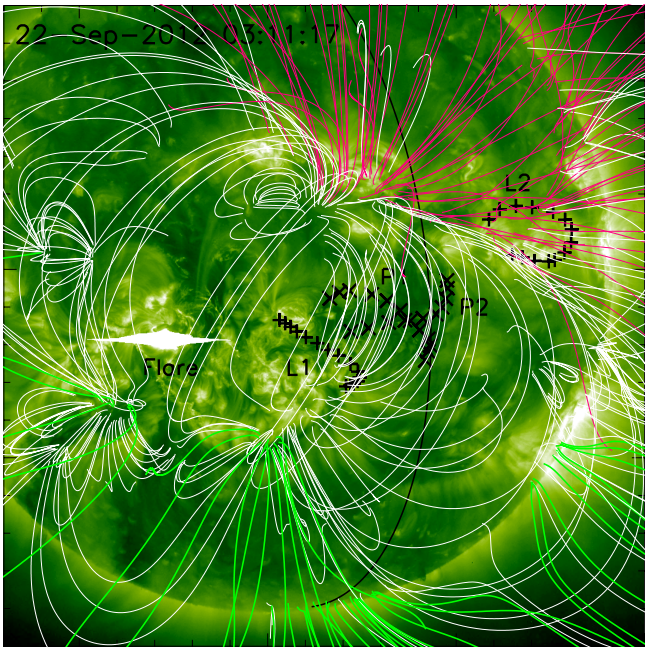

Fig. 4 Magnetic field lines generated by PFSS extrapolations (Schrijver & De Rosa 2003). The white lines correspond to closed magnetic field lines; the red and green lines correspond to open magnetic field lines. The solid black curve indicates the solar limb as seen by *SDO*. The prominences (P1, P2) are marked by the black cross symbols, and the coronal loops (L1, L2) by the black pluses.

marked as A in Figure 5; the average EM within this region, $(8.1 \pm 0.9) \times 10^{26}$ cm^{-5}, is used in Equation (3) to calculate the density in the oscillating coronal loops L1. The error of EM is also calculated by the DEM method. We assume that the LOS depth of the loop is the same as its width, which is estimated to be about 10 Mm by SCC_MEASURE. Therefore, the electron density in L1 is calculated as $n_{\rm L} = (9.0 \pm 0.5) \times 10^8$ cm^{-3}. Under the assumption that the corona is fully ionized, the mass density is $\rho_l = m_{\rm p} n_{\rm L} = (1.4 \pm 0.1) \times 10^{-15}$ g cm^{-3}, where $m_{\rm p} = 1.6 \times 10^{-24}$ g is the mass of a proton.

The method for calculating density through DEM cannot be directly used for prominences because the main parts of prominences are only observed in the low temperature 304 Å waveband, which is optically thick, and is not adequately treated by the CHIANTI model (Woods & Chamberlin 2009), on which the DEM algorithm is based. The bright structure at the prominence site in Figure 5(a) represents the high temperature corona material within the magnetic system of the prominence; i.e. only part of the prominence. Labrosse et al. (2010) concluded that the prominence plasma is typically 100 times cooler and denser than its coronal surroundings. Based on this conclusion, we select another region, marked as B in Figure 5, to calculate the density of the corona around the oscillating prominence, and then the density in P1 can be estimated. The average EM within region B is $(1.3 \pm 0.1) \times 10^{26}$ cm^{-5}. The column depth of the corona should be larger than that of the coronal loops. Here we use the pressure scale height of 1 MK plasma $H_{\rm p} \approx 60$ Mm as the column depth for the background corona. Then, the electron density in the corona around P1 is calculated to be $n_{\rm C} = (1.4 \pm 0.1) \times 10^8$ cm^{-3}, and mass density is $\rho_{\rm C} = (2.3 \pm 0.2) \times 10^{-16}$ g cm^{-3}. Therefore, the mass density of the prominence is estimated to be $\rho_P \approx (2.3 \pm 0.2) \times 10^{-14}$ g cm^{-3}.

The local magnetic field within the oscillating structures can be estimated from the densities obtained above. Kleczek & Kuperus (1969) proposed a model describing the oscillations of a prominence, where the prominence is considered as a bundle of magnetic plasma threads anchored in the photosphere, and the restoring force is considered as magnetic tension. The oscillating period of the prominence P1 is given by

$$T = 2\pi L B^{-1} \sqrt{\pi \rho}, \quad (4)$$

where L is the length of the oscillating prominence threads, ρ the mass density and B the strength of the effective magnetic field providing the restoring force. From the measured value $T = (1000 \pm 20)$ s and $L = 220$ Mm, B is calculated as (37 ± 2) Gauss, with the estimated density $\rho_P \approx (2.3 \pm 0.2) \times 10^{-14}$ g cm^{-3}. The corresponding Alfvén speed is (690 ± 70) km s^{-1}, calculated by $V_{\rm A} = B/\sqrt{4\pi\rho}$. Note that since the value of L in Table 1 is an underestimation of the length (see Sect. 3.1), the calculated B should be the lower limit of the strength of the magnetic field.

By using the phase speed of the fast kink mode, Nakariakov & Ofman (2001) calculated the local magnetic field with the parameters describing the oscillating coronal loops by

$$B = (4\pi\rho_0)^{1/2} V_{\rm A} = \frac{\sqrt{2}\pi^{3/2} L}{T} \sqrt{\rho_0 (1 + \rho_{\rm e}/\rho_0)}, \quad (5)$$

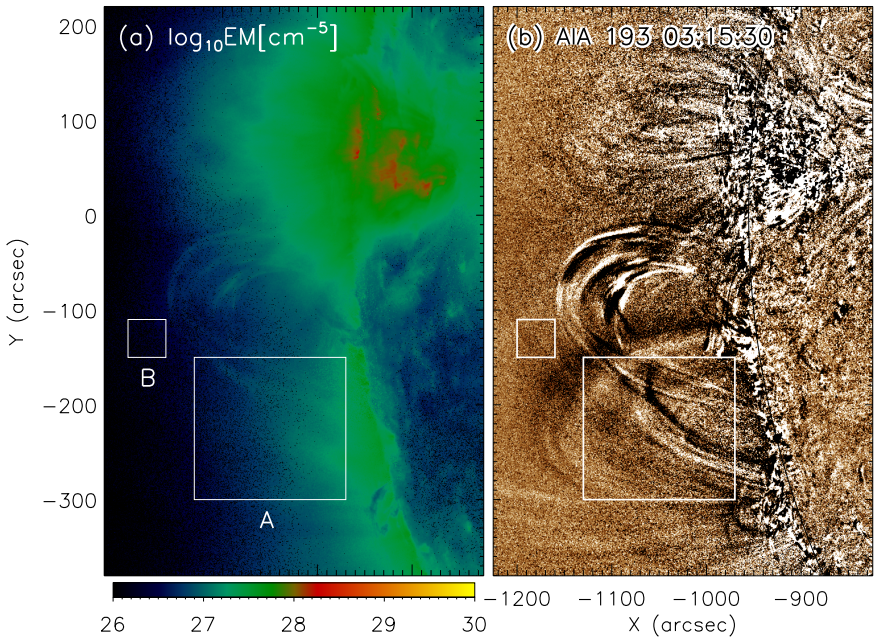

Fig. 5 DEM results to calculate the densities. Panel (a) is the distribution of logarithmic EM; panel (b) is the AIA 193 Å running difference image at the same time. The larger square, marked as A, in panels (a) and (b) indicates the region utilized to calculate the density around the oscillating coronal loops L1, and the smaller square, marked as B, is the region used for calculating the background corona.

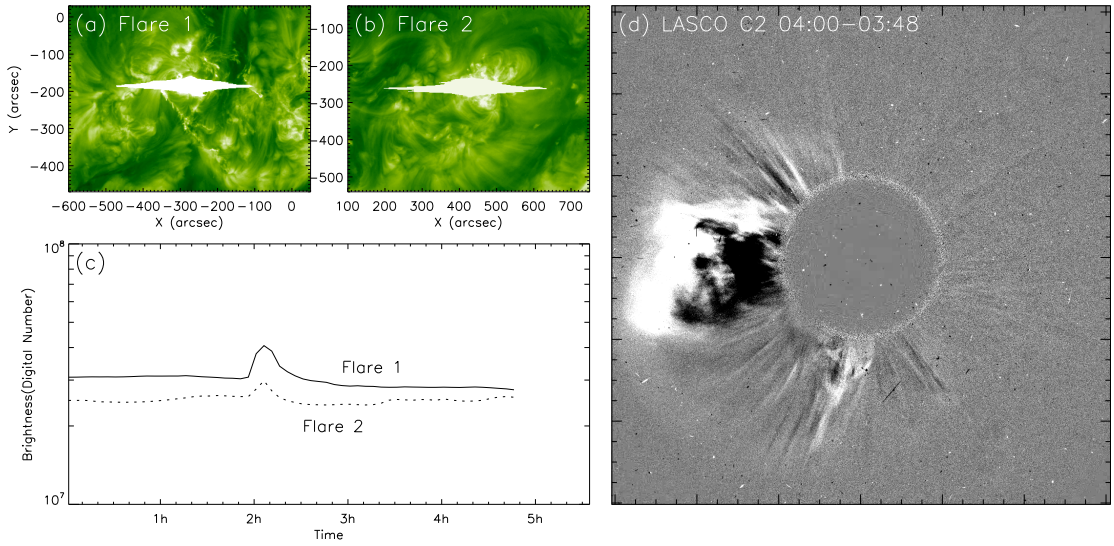

Fig. 6 The light curves of the flares. Panel (a) is the image of the flare discussed in this paper (Flare 1), whose light curve corresponds to the solid curve in panel (c). Panel (b) shows an M9.0 class flare for comparison (Flare 2), whose light curve is the dotted curve in panel (c). Panel (d) is the running difference image made from LASCO C2 observations of the CME corresponding to Flare 1.

where ρ_0 and ρ_e are the internal and external densities of the coronal loops, V_A is the Alfvén speed, L is the length of the loop and T is the period. As discussed in Section 3.1, the length of L1 cannot be directly measured from 3D reconstructions. The estimated length of the 3D reconstructed part of L1 is $L_{L1} = 220$ Mm (see Table 1), and the heights of the two 'footpoints' of the reconstructed part are 88 Mm and 122 Mm, indicating the length of L1 should be at least 430 Mm. Here we use $L = 430$ Mm, the lower limit, for L1. Assuming the external to internal density ratio to be 0.1 (Nakariakov & Ofman 2001), the magnetic field and corresponding Alfvén speed are calculated as (14 ± 1) Gauss and (1000 ± 110) km s^{-1} respectively, with $T = (960 \pm 10)$ s and $\rho_l = (1.4 \pm 0.1) \times 10^{-15}$ g cm^{-3}.

As mentioned previously, since the coronal loops L1 oscillated in a cylindrical kink mode, the damping time scale of the oscillation can also be used to calculate the local physical parameters. By comparing the damping time scaling predicted by several damping mechanisms with that of the transverse oscillations in 26 coronal loops from 17 events, Ofman & Aschwanden (2002) demonstrated that the damping power index predicted by phase mixing is in excellent agreement with the observation, superior to other mechanisms. Then, according to the phase mixing model deduced by Roberts (2000), the e-folding damping time of the oscillation $\tau_{\rm decay}$ is given by

$$\tau_{\rm decay} = \left(\frac{6L^2 l^2}{\nu \pi^2 V_{\rm A}^2} \right)^{\frac{1}{3}}, \quad (6)$$

where L, l, ν and $V_{\rm A}$ correspond to the length of the coronal loop (the same as that in Eq. (5)), scale of the inhomogeneity across the loop, the coronal viscosity and Alfvén speed, respectively, and $\tau_{\rm decay}$ for L1 has been calculated to be (1300 ± 100) s (see Sect. 3.3). By assuming $l = 0.01L$ and $\nu = 4 \times 10^{13}$ cm^2 s^{-1} (Roberts 2000), the Alfvén speed $V_{\rm A}$ is calculated to be (480 ± 60) km s^{-1}, and the corresponding magnetic field is (6.4 ± 0.9) Gauss, which is comparable to the field strength given by the phase speed of the fast kink mode. The difference between the estimations of the magnetic fields by the phase speed of the fast kink mode and by phase mixing might result from the underestimation of the length of L1 ($B \sim L$ in Eq. (5) and $B \sim V_{\rm A} \sim L^2$ in Eq. (6), so that with increasing L, the difference between values calculated from Eq. (5) and Eq. (6) will decrease).

3.5 Propagating Height of the Wave

Since the oscillations are triggered by the coronal wave, the different responses to the wave passage of different structures in different locations shed light on the nature of the coronal wave. Besides oscillating P1 and L1, two non-oscillating structures P2 and L2 were also present (see Sect. 3.1 and the animation accompanying Fig. 3). In order to analyze the propagation of the wave, potential-field source-surface (PFSS; Schatten et al. 1969) extrapolation is introduced to illustrate the magnetic configurations around the structures of interest. Full-Sun PFSS extrapolation results from 04:00 UT on 2012 September 22 are shown in Figure 4. Since the relevant structures were located near the solar limb, PFSS extrapolations at the regions of these structures are based on data a week later or two weeks earlier. On the other hand, the magnetic fields around the prominences and the loops might be non-potential. As a result, PFSS results deviate from the detailed observed 3D structures. Here, we only use PFSS to trace magnetic field lines at high altitude, which represents the external large-scale magnetic field over the relevant structures. Based on the traced external magnetic configuration, we could analyze the propagation of the wave. Wang (2000) concluded that coronal waves are deflected away from active regions and coronal holes, where the velocity of the fast-mode magnetohydrodynamic wave is large. Thus, the PFSS result reveals that the coronal wave could propagate through the region of L1, P1 and P2. However, L2 was located in the region surrounded by open magnetic fields, which will prevent the coronal wave passage, resulting in the non-oscillating behavior of L2.

Figure 4 reveals that P2, although at a lower altitude (see Table 1), was located at almost the same region as P1, under the same group of magnetic arcades. This indicates that the responses of P1 and P2 to the wave should not vary that much. As shown in Figure 3(d), however, the threads in P1 began to oscillate after the wave passage, whereas there were no obvious motions along slit-1 in P2. As demonstrated above, large-amplitude oscillations in P1 were triggered by the wave. This indicates that the compression of the wave should be strong. Thus, if the wave had propagated through P2, at least disturbances along slit-1, i.e. the same direction as the oscillation in P1, should be triggered in P2 by the wave. Note that both P1 and P2 were located near the solar limb from the perspective of *SDO*, so that the projection effect is small. The fact that no disturbances were detected along the slit in P2 after the wave passage indicates that there might be no interaction between the wave and P2. This should result from the different altitudes of P1 and P2. Therefore, we may conclude that the wave must propagate above a certain height; i.e., the lower boundary of the wave front is between 50 Mm and 130 Mm, the maximum heights of P2 and P1, respectively. A similar conclusion was also reached by Liu et al. (2013), in which the lowest of the four filaments did not respond to the Moreton wave. By triangulations of the wave front, Patsourakos et al. (2009) found that the height of the wave above the solar surface was about 90 Mm. Kienreich et al. (2009) also suggested that the coronal wave originated from 80–100 Mm above the solar surface with the *STEREO* quadrature observations. Different from those studies, the flare site in this paper is far behind the solar limb from the perspective of Earth. As a result, the wave front can hardly be observed in AIA images, so that the methods utilized above are infeasible here. Our result, obtained from interactions between the wave and prominences, is consistent with previous studies. Such heights are comparable to the coronal scale heights for the quiet Sun, which are 50$\sim$100 Mm for temperatures of 1$\sim$2 MK. Patsourakos et al. (2009) concluded that the fast-mode wave perturbs the ambient coronal plasma with its bulk confined within a coronal scale height, also indicating that our observation is consistent with the fast-mode wave propagation.

4 DISCUSSION AND CONCLUSIONS

As discussed above, the oscillations in P1 and L1 were triggered by the coronal wave. The exact nature of the relationship between the properties of the wave and the filament activation is currently not well understood (Tripathi et al. 2009). However, we may still conclude that the wave

energy deposited in P1 and L1 should be no less than the oscillating energies of P1 and L1, respectively. The oscillating energies can be estimated from the oscillating parameters

$$E = \frac{1}{2}mv_{\rm max}^2 = \frac{2\pi^2 mA^2}{T^2},\ m = \rho\pi r^2 L, \qquad (7)$$

where m, A, T, ρ, r and L correspond to the mass, amplitude, oscillating period, mass density, radius and length of the prominence (coronal loops), respectively. Assuming $r = 10$ Mm for the prominence threads, the same as that of L1, the oscillating energies can be estimated from the measured values of A, T, L and ρ in Section 3.3 and Section 3.4: the oscillating energy of the prominence P1 is $E_{\rm P1} = (1.0 \pm 0.4) \times 10^{28}$ erg and the energy of the loops L1 is $E_{\rm L1} = (1.6 \pm 0.3) \times 10^{28}$ erg. Therefore, the lower limit of the dissipated wave energy within the region of P1 and L1 is $\Delta E = E_{\rm P1} + E_{\rm L1} \sim 10^{28}$ erg. P1 and L1 span about 30 deg with respect to the flare, as shown by the area outlined in black in the bottom left panel of Figure 1, and only the wave within this sector interacted with P1 and L1. Since coronal waves are generally considered to be isotropic and propagate over a wide area almost symmetrically relative to the flare site (Chertok & Grechnev 2003; Warmuth et al. 2001; Nakariakov & Verwichte 2005), the total energy of the wave should be much larger than the deposited wave energy within P1 and L1, probably of the order of $10^{29} \sim 10^{30}$ erg.

Since the relevant flare is behind the solar limb, there are no GOES observations for it. Figure 6(c) exhibits the comparison between the light curves of the flare of interest (Flare 1) and an M9.0 flare that occurred on 2012 October 20 (Flare 2), in order to roughly estimate the class of the relevant flare. These light curves are both generated from EUVI 195 Å direct images within a 650×500 arcsec region, as shown in Figure 6(a) and 6(b). Although the backgrounds of these two flares were different, the increase of the peak value during Flare 1 relative to the background (the average value before the onset of the flare) is 1.0×10^7 dn, and that during Flare 2 is 3.7×10^6 dn. It is obvious that the M9.0 flare should be less energetic than Flare 1, indicating that Flare 1 might be a large flare, probably an X class one. Thus, the total energy released by the relevant flare should be of the order of $E_{\rm flare} = 10^{32}$ erg (Tandberg-Hanssen & Emslie 2009). Aschwanden et al. (2014) also demonstrated that the magnetic free energies of large flares are usually larger than 10^{31} erg. Therefore, the flare energy is much larger than the estimated wave energy. The direct trigger for coronal waves, at least those that have a bright wave front, are usually considered to be Coronal Mass Ejections (CMEs) (Biesecker et al. 2002; Ballai et al. 2005; Chen 2006). In this event, a CME was generated by the flare, as shown in Figure 6(d), which is an observation from the Large Angle and Spectrometric Coronagraph (LASCO; Brueckner et al. 1995) on board *SOHO*. From the the LASCO CME list on the website of the CDAW Data Center, the kinetic parameters of the CME are as follows: the velocity of the CME is 774 km s^{-1} and the kinetic energy is 2.7×10^{31} erg, which is also much larger than the estimated wave energy. Therefore, we conclude that the flare and the corresponding CME should be energetic enough to trigger the coronal wave.

In summary, we quantitatively investigate the oscillations, triggered by a global coronal wave, of the prominence and the coronal loops. Local physical parameters are obtained from the observed oscillating properties. The magnetic field strength and the Alfvén speed of the prominence are at least about 37 Gauss and 690 km s^{-1}, while those of the coronal loops are 6∼14 Gauss and 480∼1000 km s^{-1} respectively. By comparing the locations and heights of the oscillating and non-oscillating structures, the propagating height of the wave is estimated to be 50∼130 Mm, comparable to the coronal scale heights for the quiet Sun. Finally, the lower limit of the energy dissipations of the coronal wave are roughly gauged by the oscillating energies, and the relevant flare and CME are demonstrated to be energetic enough to trigger this coronal wave. The 3D reconstructions play an important role in analyzing the observations. Oscillations can not only be used in coronal seismology but can also reveal the properties of the wave.

Acknowledgements This research is supported by the National Natural Science Foundation of China (Grant Nos. 41131065, 41574165, 41421063 and 41304134), MOEC (20113402110001), CAS Key Research Program (KZZD-EW-01-4), the fundamental research funds for the central universities (WK2080000077), and the foundation for Young Talents in College of Anhui Province (2013SQRL044ZD). The CME catalog used to obtain the kinetic parameters of the relevant CME is generated and maintained at the CDAW Data Center by NASA and The Catholic University of America in cooperation with the Naval Research Laboratory. *SOHO* is a project of international cooperation between ESA and NASA.

References

Arregui, I., Andries, J., Van Doorsselaere, T., Goossens, M., & Poedts, S. 2007, A&A, 463, 333

Arregui, I., Oliver, R., & Ballester, J. L. 2012, Living Reviews in Solar Physics, 9, 2

Aschwanden, M. J., & Acton, L. W. 2001, ApJ, 550, 475

Aschwanden, M. J., de Pontieu, B., Schrijver, C. J., & Title, A. M. 2002, Sol. Phys., 206, 99

Aschwanden, M. J., Fletcher, L., Schrijver, C. J., & Alexander, D. 1999, ApJ, 520, 880

Aschwanden, M. J., Xu, Y., & Jing, J. 2014, ApJ, 797, 50

Ballai, I., Erdélyi, R., & Pintér, B. 2005, ApJ, 633, L145

Biesecker, D. A., Myers, D. C., Thompson, B. J., Hammer, D. M., & Vourlidas, A. 2002, ApJ, 569, 1009

Brueckner, G. E., Howard, R. A., Koomen, M. J., et al. 1995, Sol. Phys., 162, 357

Chen, P. F. 2006, ApJ, 641, L153

Chertok, I. M., & Grechnev, V. V. 2003, Astronomy Reports, 47, 139
Cranmer, S. R., van Ballegooijen, A. A., & Edgar, R. J. 2007, ApJS, 171, 520
Delaboudinière, J.-P., Artzner, G. E., Brunaud, J., et al. 1995, Sol. Phys., 162, 291
Gilbert, H. R., Daou, A. G., Young, D., Tripathi, D., & Alexander, D. 2008, ApJ, 685, 629
Goossens, M., Andries, J., & Aschwanden, M. J. 2002, A&A, 394, L39
Gopalswamy, N., Yashiro, S., Temmer, M., et al. 2009, ApJ, 691, L123
Hannah, I. G., & Kontar, E. P. 2012, A&A, 539, A146
Hershaw, J., Foullon, C., Nakariakov, V. M., & Verwichte, E. 2011, A&A, 531, A53
Heyvaerts, J., & Priest, E. R. 1983, A&A, 117, 220
Howard, R. A., Moses, J. D., Vourlidas, A., et al. 2008, Space Sci. Rev., 136, 67
Isobe, H., & Tripathi, D. 2006, A&A, 449, L17
Isobe, H., Tripathi, D., Asai, A., & Jain, R. 2007, Sol. Phys., 246, 89
Kaiser, M. L., Kucera, T. A., Davila, J. M., et al. 2008, Space Sci. Rev., 136, 5
Kienreich, I. W., Temmer, M., & Veronig, A. M. 2009, ApJ, 703, L118
Kleczek, J., & Kuperus, M. 1969, Sol. Phys., 6, 72
Kumar, P., Cho, K.-S., Chen, P. F., Bong, S.-C., & Park, S.-H. 2013, Sol. Phys., 282, 523
Labrosse, N., Heinzel, P., Vial, J.-C., et al. 2010, Space Sci. Rev., 151, 243
Lemen, J. R., Title, A. M., Akin, D. J., et al. 2012, Sol. Phys., 275, 17
Li, T., & Zhang, J. 2012, ApJ, 760, L10
Liu, R., Liu, C., Xu, Y., et al. 2013, ApJ, 773, 166
Liu, W., Ofman, L., Nitta, N. V., et al. 2012, ApJ, 753, 52
Nakariakov, V. M., & Ofman, L. 2001, A&A, 372, L53
Nakariakov, V. M., Ofman, L., Deluca, E. E., Roberts, B., & Davila, J. M. 1999, Science, 285, 862
Nakariakov, V. M., & Verwichte, E. 2005, Living Reviews in Solar Physics, 2, 3
Ofman, L., & Aschwanden, M. J. 2002, ApJ, 576, L153
Ofman, L., & Thompson, B. J. 2002, ApJ, 574, 440
Okamoto, T. J., Nakai, H., Keiyama, A., et al. 2004, ApJ, 608, 1124
Oliver, R. 2009, Space Sci. Rev., 149, 175
Oliver, R., & Ballester, J. L. 2002, Sol. Phys., 206, 45
Patsourakos, S., Vourlidas, A., Wang, Y. M., Stenborg, G., & Thernisien, A. 2009, Sol. Phys., 259, 49
Pesnell, W. D., Thompson, B. J., & Chamberlin, P. C. 2012, Sol. Phys., 275, 3
Roberts, B. 2000, Sol. Phys., 193, 139
Ruderman, M. S. 2005, in ESA Special Publication, 600, The Dynamic Sun: Challenges for Theory and Observations, 96.1
Ruderman, M. S., & Roberts, B. 2002, ApJ, 577, 475
Schatten, K. H., Wilcox, J. M., & Ness, N. F. 1969, Sol. Phys., 6, 442
Schrijver, C. J., Aschwanden, M. J., & Title, A. M. 2002, Sol. Phys., 206, 69
Schrijver, C. J., & Brown, D. S. 2000, ApJ, 537, L69
Schrijver, C. J., & De Rosa, M. L. 2003, Sol. Phys., 212, 165
Tandberg-Hanssen, E., & Emslie, A. G. 2009, The Physics of Solar Flares (Cambridge: Cambridge Univ. Press)
Thompson, B. J., Gurman, J. B., Neupert, W. M., et al. 1999, ApJ, 517, L151
Tripathi, D., Isobe, H., & Jain, R. 2009, Space Sci. Rev., 149, 283
Veronig, A. M., Muhr, N., Kienreich, I. W., Temmer, M., & Vršnak, B. 2010, ApJ, 716, L57
Vršnak, B., Veronig, A. M., Thalmann, J. K., & Žic, T. 2007, A&A, 471, 295
Wang, Y.-M. 2000, ApJ, 543, L89
Warmuth, A., Vršnak, B., Aurass, H., & Hanslmeier, A. 2001, ApJ, 560, L105
Woods, T. N., & Chamberlin, P. C. 2009, Advances in Space Research, 43, 349
Wuelser, J.-P., Lemen, J. R., Tarbell, T. D., et al. 2004, in Proc. SPIE, 5171, Telescopes and Instrumentation for Solar Astrophysics, eds. S. Fineschi, & M. A. Gummin, 111
Zhang, Q., Liu, R., Wang, Y., et al. 2014, ApJ, 789, 133